1s2p Resonant Inelastic X-ray Scattering of Iron Oxides

Frank M. F. de Groot,*,† Pieter Glatzel,‡ Uwe Bergmann,§ Peter A. van Aken,‖ Raul A. Barrea,⊥ Stephan Klemme,# Michael Hävecker,▽ Axel Knop-Gericke,▽ Willem M. Heijboer,† and Bert M. Weckhuysen†

Department of Inorganic Chemistry and Catalysis, Debye Institute, Utrecht University, Sorbonnelaan 16, 3584 CA Utrecht, The Netherlands, European Synchrotron Radiation Facility, BP 220, F-38043 Grenoble Cedex, France, Stanford Synchrotron Radiation Laboratory, 2575 Sand Hill Road, Menlo Park, California 94025, Institut für Angewandte Geowissenschaften, Technische Universität Darmstadt, Schnittspahnstrasse 9, 64287 Darmstadt, Germany, Argonne National Laboratory, Advanced Photon Source, BioCAT, Argonne, Illinois 60439, Mineralogisches Institut, Universität Heidelberg, Im Neuenheimer Feld 236, 69120 Heidelberg, Germany, and Fritz-Haber-Institut der Max-Planck-Gesellschaft, Faradayweg 4-6, D-14195 Berlin, Germany

Received: July 20, 2005; In Final Form: September 7, 2005

1s2p resonant inelastic X-ray scattering (RIXS) spectroscopy has been measured for a series of iron oxides, including octahedral and tetrahedral Fe^{II} and Fe^{III} systems. Their spectral shapes have been analyzed and explained using crystal-field multiplet simulations. The RIXS planes and the K-edge and L-edge X-ray absorption spectra related to these RIXS planes will be discussed with respect to their analytical opportunities. It is concluded that the full power and possibilities of 1s2p RIXS needs an overall resolution of 0.3 eV. This will yield a technique with more detailed information than K-edge and L-edge X-ray absorption combined, obtained in a single experiment. Another major advantage is that 1s2p RIXS involves only hard X-rays, and experiments under essentially any condition and on any system are feasible.

1. Introduction

Over the past two decades, both K-edge and L-edge absorption of the 3d transition metals have developed into important characterization techniques in many fundamental and applied research fields, including, for example, surface chemistry,[1] coordination chemistry,[2] and metalloproteins.[3] The K edges of 3d transition metals are found in the hard X-ray regime between 5 and 10 keV and are measured routinely under essentially any condition, for example, under reaction conditions for catalysts, in cryostats for proteins, and in diamond anvil cells for high-pressure studies. The possibility of reaching more extreme conditions and obtaining spectra on, for example, proteins with a much reduced radiation dose has given K-edge X-ray absorption a big advantage over the soft X-ray L-edges. A major disadvantage of K edges is the intrinsic broadening due to the 1s lifetime broadening of 1−2 eV, some three times broader than the corresponding L edges. This large broadening blurs many details, and this disadvantage means that K edges are usually less informative than the corresponding L edges. Another difference between K and L edges is that L edges probe directly the 3d-states at the valence band. The partially filled and correlated 3d-states are at the basis of the most interesting properties of 3d metals: their catalytic performance, magnetic coupling, and redox properties. The K edges probe, in the dipole approximation, only the empty metal 4p-states, which give less direct information on the ground state properties. It turns out that at the metal K-edges, the quadrupole transitions directly into the 3d band are not negligible, but these transitions, visible as preedge structures before the main K edge, are difficult to analyze. There are at least two main reasons for their obscurity: (1) the lifetime broadening and usually the applied experimental resolution yield a total broadening on the order of 1.5 eV, blurring much of the potential fine structure in the preedges and (2) it turns out that the preedge consists of both direct quadrupole transitions and dipole transitions to p-character that has hybridized with the 3d band. As a result, the preedge structures are in most cases analyzed only qualitatively. Alternatively, they are analyzed in a more phenomenological manner by measuring global properties (i.e., their center gravity and integrated intensity) to relate to properties such as their site symmetry and effective mean valence.[4]

The L edges of 3d transition metals are found in the soft X-ray regime between 400 and 1000 eV and are measured routinely under vacuum conditions. There are actually two main routes for measuring these metal edges: (1) using a soft X-ray absorption (XAS) beamline at a storage ring and (2) using a dedicated transmission electron microscope (TEM) equipped with an electron energy loss (EELS) spectrometer. Soft X-ray beamlines have a typical resolution better than 0.1 eV, and TEM-EELS machines have a resolution in the range of 0.2[5] to 0.6 eV,[6] which is in the same range as the lifetime broadening of the 2p core holes, ranging from 0.2 eV[7] to 0.5 eV (fwhm).[8] TEM microscopes use electrons of typically 100 or 200 keV, and only samples with a thickness of less than 100 nm are easy to measure. Soft X-rays penetrate solids a few micrometers, but the main detection technique is total electron yield (TEY), where the electrons have an escape depth of only a few nanometers. A disadvantage of both TEY-XAS and TEM-EELS is that both usually need vacuum conditions to perform the experiments.

* Corresponding author. E-mail: f.m.f.degroot@chem.uu.nl.
† Debye Institute.
‡ European Synchrotron Radiation Facility.
§ Stanford Synchrotron Radiation Laboratory.
‖ Technische Universität Darmstadt.
⊥ Argonne National Laboratory.
Universität Heidelberg.
▽ Fritz-Haber-Institut der Max-Planck-Gesellschaft.

10.1021/jp054006s CCC: $30.25
Published on Web 10/13/2005

The reason for the vacuum is that both techniques measure the number and energy of electrons escaping from the surface of the samples and these electrons interact strongly with air. Large efforts are made to move both TEY-SXAS and TEM-EELS into in-situ conditions, but for both techniques the present status is that the upper limit for the pressure is in the millibar range.[9,10] A few setups exist that go to higher pressures, for example, fluorescence yield XAS.[11]

In resonant inelastic X-ray scattering (RIXS) spectroscopy, a secondary monochromator (analyzer) with an energy bandwidth on the order of the lifetime broadening is used as a fluorescence detector. The first application of RIXS for 3d metal systems has been the effective removal of the 1s lifetime broadening, allowing the measurement of the K edge (or more precisely, a K-edge-like structure; see the discussion below) with unprecedented resolution.[12] Since then, a number of applications of RIXS have been developed and demonstrated, for example, the measurement of the spin-selective K edges, valence-selective EXAFS, and range-extended EXAFS by using detection channels specific for a certain edge, valence, and/or spin state.[2,13]

The electronic states that form the edge of an absorption spectrum are resonantly excited states that subsequently decay. In the case of a 3d transition metal ion, the radiative decay with the highest probability after 1s core hole creation is a 2p to 1s transition or the Kα fluorescence emission. The spectroscopy is therefore denoted 1s2p RIXS to describe the core hole in the intermediate (1s) and final (2p) state. The fluorescence light emitted during the decay process can be recorded using a crystal analyzer with an energy bandwidth similar to that of the primary monochromator of the synchrotron beamline.[14] The process can be viewed as an inelastic scattering of the incident photon at the 3d transition metal atom and is theoretically described by the Kramers−Heisenberg formula[15]

$$F(\Omega,\omega) = \sum_f \left| \sum_n \frac{\langle f|T_2|n\rangle\langle n|T_1|g\rangle}{E_g - E_n + \Omega - i\frac{\Gamma_K}{2}} \right|^2 * \frac{\frac{\Gamma_f}{2\pi}}{(E_g - E_f + \Omega - \omega)^2 + \frac{\Gamma_f^2}{4}} \quad (1)$$

The intermediate state, $|n\rangle$, is reached from the ground state, $|g\rangle$, via a transition operator, T_1. In a simplified picture using atomic configuration for Fe^{III}, we can write $|g\rangle = 3d^5$ and $|n\rangle = 1s3d^6$; that is, a 1s electron is resonantly excited into a 3d orbital. The intermediate states, $|n\rangle$, in RIXS spectroscopy are the final states in conventional K-edge absorption spectroscopy.

The final states are reached via a 2p to 1s transition, and T_2 therefore identifies with the dipole operator. The 1s2p RIXS final state configuration $|f\rangle = 2p^53d^6$ is identical to the final state configuration in soft X-ray L-edge absorption spectroscopy. Transition metal L-edge spectra with their pronounced chemical sensitivity have been discussed in depth by numerous authors.[1,16] In particular, it was found that the strong (2p,3d) multiplet interaction makes the L edge more sensitive to the metal spin state. The same interaction also occurs in the 1s2p RIXS final states.

The incident energy, Ω, as well as the emitted energy, ω, is varied in a RIXS experiment. The recorded intensity is proportional to $F(\Omega,\omega)$ (cf. eq 1) and is thus plotted versus a 2D grid: the RIXS plane. To assign the total energy of electronic states to the axes of the contour plots, one uses the incident energy axis, Ω (intermediate state energy), and the energy transfer axis, $\Omega-\omega$ (final state energy). This choice of axes of the RIXS plane has also the advantage of the energy transfer axis relating to the excitation energy in L-edge absorption spectroscopy. The Kramers−Heisenberg equation contains two Lorentzian line shapes for the incident energy and the energy transfer. The lifetime broadenings, Γ_K for the intermediate states and Γ_L, for the final states thus apply in the Ω and $\Omega-\omega$ direction, respectively. An experimental spectrum is further broadened by the energy bandwidths of the incident energy monochromator and the crystal analyzer.

Caliebe and co-workers performed 1s2p RIXS experiments on Fe_2O_3, and they measured the 1s2p RIXS spectra at the peak positions of the preedge structure. They derived 1s2p RIXS spectra that were equivalent to direct 2p-XAS spectra.[17] In this paper, we discuss the potential of 1s2p RIXS for the analysis of 3d metals including experimentally obtained 2D energy grids and a detailed theoretical analysis. As an example, we use four iron oxides, Fe_2O_3, $FeAl_2O_4$, $FePO_4$, and Fe_2SiO_4, respectively, octahedral Fe^{III}, octahedral Fe^{II}, tetrahedral Fe^{III}, and tetrahedral Fe^{II}. With these four oxides, we cover the four main iron sites in oxide systems. Octahedral systems are expected to have a K preedge structure that is completely dominated by direct quadrupole transitions,[18] whereas tetrahedral systems have significant 3d4p admixture leading to mixed dipole and quadrupole contributions. All spectra will be analyzed using the crystal-field multiplet code. The K preedge structure will be simulated using quadrupole 1s3d transitions. Using exactly the same ground state, the L edges will be calculated using the 2p3d dipole transitions. Finally, the complete 1s2p RIXS spectrum will be calculated using the Kramers−Heisenberg formula and both the 1s3d quadrupole excitation (intermediate state) coupled to the 1s2p dipole decay (final state).

The use of 2D images has been introduced in the hard X-ray range for a series of nickel compounds.[19] The cross sections through these images showed very interesting effects. The cross sections measured at constant incident energy (CIE) showed L-edge-like spectra, similar to those obtained by Caliebe et al.[17] In addition, the cross sections measured at constant emitted energy (CEE) showed sharpened versions of the K preedges. This has been applied to a series of Fe/ZSM5 catalysts, that is, iron-oxide complexes in a zeolite matrix.[20] Below we will systematically compare the various cross sections that are possible. Recently, a series of manganese compounds[21] and a number of iron oxides[22] have been studied in a similar fashion. Rueff and co-workers measured a series of iron oxides and analyzed the preedge 1s2p RIXS.

In the present paper, we add the theoretical multiplet calculations, with which it becomes possible to interpret preedge structures and the 1s2p RIXS spectra in a quantitative way and to probe which physical phenomenon is at the origin of the various peaks and structures. We limit ourselves to crystal-field multiplet calculations, and we will show that these calculations capture the main trends and effects that are observed, although additional effects remain that will be mentioned in the discussion.

The most general way to present RIXS is by showing 2D plots that provide a comprehensive picture of the 1s X-ray absorption and the 1s2p X-ray emission processes. For quantitative purposes it is, however, more convenient to compare 1D spectral shapes. There are a number of ways one can create

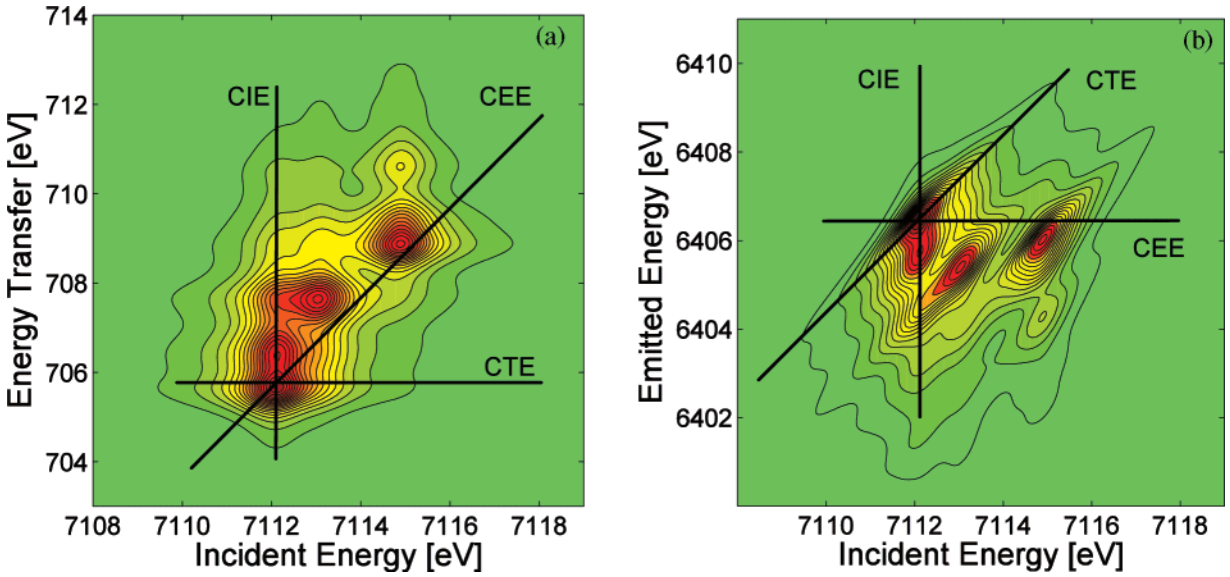

Figure 1. Two-dimensional contour plot of a theoretical $1s2p_{3/2}$ RIXS spectrum for Fe^{II} using an experimental broadening of 0.3 eV for both the monochromator and the detector resolution. The contour plots indicate lines of equal intensity where the dark (red) areas have the highest intensity. The difference between the two plots is that in plot a the vertical axis gives the energy transfer ($\Omega-\omega$) and in plot b it gives the emitted energy (ω). The lines indicate the three different cross sections, CIE, CEE, and CTE, as discussed in the text.

spectral shapes out of the 2D images. In Figure 1, we illustrate the three most straightforward cross sections. These are the following, respectively: constant incident energy (CIE) spectra, a vertical cross section at fixed excitation energy (7112 eV in Figure 1a and b). This relates to resonant X-ray emission spectra. Constant transferred energy (CTE) spectra, a horizontal cross section at a constant transferred energy in Figure 1a. In Figure 1b, the CTE scan is a diagonal cross section. A constant transferred energy implies that for all excitation energies the same final states are probed. This could also be called constant final state (CFS) spectra, but we prefer an experimental nomenclature. Constant emission energy (CEE) spectra: a diagonal cross section at a constant emission energy in Figure 1a. In Figure 1b, the CEE scan is a horizontal cross section at fixed emission energy. This relates to the so-called "lifetime removed" or "lifetime suppressed" spectra. These scans are sometimes referred to as partial fluorescence yield (PFY). Here, as well, we prefer the exact reference to the experimental procedure in the acronym because the emission energy of the fluorescence line can shift depending on the excitation energy.

In addition to these three cross sections, spectra can be measured (or created from a 2D image) with a broader line width. In the limit that the complete preedge structure is included in such broad line scans, one can call them integrated spectra. This gives the following: integrated incident energy (IIE) spectra, a vertical band centered around a fixed excitation energy in Figure 1a and b. This yields the total decay intensity of all intermediate states to the 2p final states. Integrated transferred energy (ITE) spectra, a horizontal band centered around a transferred energy in Figure 1a. In Figure 1b, the ITE scan is a diagonal band. Effectively, this implies that the complete decay at a certain excitation energy is integrated; in other words, this relates to total fluorescence yield. Integrated emission energy (IEE) spectra, a diagonal band centered around constant emission energy in Figure 1a. In Figure 1b, the CEE scan is a horizontal band. Effectively, this also implies that the complete decay at a certain excitation energy is integrated; in other words, this also relates to total fluorescence yield. Note that with both an ITE scan and an IEE scan the same spectrum is created as long as the complete preedge is integrated. Note that the behavior of ITE scans and IEE scans is different above the edge where IEE scans follow the normal fluorescence and as such relate to the total Kα fluorescence yield.

The principle of these cross sections and integrated spectra is clear, but it might not be obvious which type of line scan is most significant for the determination of the electronic structure of the system under study. One can, for example, argue that absorption-like spectra (ITE, CTE, and CEE) are more direct because they relate to transitions from the ground state. IIE and CIE are related to X-ray emission spectra and yield more indirect information. However, in a 1s2p RIXS experiment the 2p final state has strong multiplet features and always less lifetime broadening. Hence, there is potentially more information in IIE and CIE spectra, where one essentially measures 2p-XAS-like spectra using hard X-rays. In section 3.1, we will discuss the 2D images, which are compared to K edges in section 3.2 and to L edges in section 3.3.

2. Experimental Section

2.1. 1s2p RIXS. RIXS data were recorded on the Bio-CAT undulator beamline 18-ID at the Advanced Photon Source.[23] The energy of the incoming synchrotron beam was selected by means of a nitrogen-cooled Si (1,1,1) double-crystal monochromator. The sample was oriented at 45° relative to the incident beam, and the beam size on the sample was 1.5 mm horizontal and 0.5 mm vertical fwhm. The focusing mirror rejected higher harmonics. Using the fundamental undulator peak, the maximum incident flux was $\sim 10^{13}$ photons/sec at 7.1 keV. For some samples, Al foils attenuated the incident beam intensity to prevent detector saturation and/or sample radiation damage. The incident X-ray monochromator energy bandwidth was less than 1.0 eV at 7100 eV. The monochromator was operated in continuous scan mode, where data are acquired "on the fly" during motor motion, thus minimizing the dead time per scan. A beam shutter was inserted automatically when no data were acquired during motor motions (monochromator or sample positioning) to reduce sample illumination. The monochromator energy calibration was checked repeatedly by recording the K-edge of an Fe foil at 7112 eV.

The scattered/emitted X-rays were collected by means of a crystal array spectrometer as described in detail elsewhere.[24]

The (4,4,0) Bragg reflection of four spherically bent ($R = 1000$ mm) Ge crystals of 89 mm diameter each arranged in Rowland geometry were used. The analyzer crystals captured a solid angle of 3.4×10^{-2} sr. A nitrogen-cooled solid state (Ge) detector was placed at the common focus of the four crystals, and the entire emitted beam path was enclosed by a He-filled bag. The narrow energy bandwidth of the Ge detector ($\sim$300 eV at 6.5 keV) was used to window out unwanted X-ray events and thus improved the signal-to-background ratio. The energy bandwidth of the emission spectrometer was better than 0.5 eV as determined by measuring the elastic peak at 6504 eV Energy calibration of the spectrometer was achieved by measuring the absolute angle of the Bragg reflection using optical tools. We estimate that the upper limit for the error of the absolute energy calibration is 1 eV.

In our setup, the intersecting Rowland circles are oriented perpendicular to the synchrotron plane in the vertical direction. Therefore, changes in energy are most sensitive to vertical movements of the synchrotron beam, which can affect the energy calibration of the spectrometer. By using a guard slit in front of the sample, the vertical position of the spectrometer source volume was fixed and we give an upper limit for the absolute error of the energy transfer of 0.1 eV. Scans of the scattered X-rays were taken between 6395 and 6413 eV, corresponding to Bragg angles of 75.78 and 75.15 degrees, respectively. Energy scans of the scattered X-rays were achieved by simultaneously moving the table holding the analyzer crystals and the detector (twice the amount) in the vertical direction.[24] The table step size was 0.05 mm, which translates to energy steps of 0.081 eV at 6395 and 0.085 eV at 6413 eV on the energy transfer axis. The count rates in the continuous monochromator scans were integrated over steps of 0.1 eV.

High-resolution $K\alpha_1$-detected XANES spectra were recorded by tuning the analyzer energy to the maximum intensity of the Fe $K\alpha_1$ emission peak of Fe_2O_3 and by scanning the incident energy through the XANES region. This procedure is referred to as a constant emission energy (CEE) scan and corresponds to a diagonal line scan through the (Ω, $\Omega-\omega$) RIXS plane. The XANES spectra were normalized by the average absorption intensity, determined at around 7200 eV

Radiation damage studies were performed for all samples by recording $K\alpha_1$-detected CEE scans. The beam position on the sample could be adjusted vertically and horizontally, and the total illumination time per sample position was kept below the time limit when damage occurred. To obtain the two-dimensional RIXS plane, we recorded CEE scans while the fluorescence energy changed stepwise. We took a total of 221 CEE scans for the model compounds to build up the experimental RIXS planes. The beam position on the sample was changed with every scan and the maximum scan time was 30 s. To correct for Fe concentration variations across the sample, we measured the scattered X-ray intensity at a constant incident energy chosen at the preedge absorption maximum for each sample position. Each CEE scan was corrected for variations in the incident intensity, I_0, and all CEE scans that form a RIXS plane were corrected relative to each other with respect to I_0 and Fe concentration variations across the sample. The experimental RIXS plane was splined on an energy grid with equal energy steps of 0.1 eV in both directions. A constant background was subtracted from all RIXS spectra. All of the samples were measured as powders at room temperature. To minimize fluorescence saturation,[25] the samples were made optically thin by diluting the pure sample with boron nitride.

2.2. In Situ Soft X-ray Absorption Spectroscopy. The soft X-ray absorption spectra of the Fe $L_{2,3}$ edge (700−730 eV) of Fe_2O_3 and $FePO_4$ were measured at BESSY (Berlin) using beamline U49/2-PGM-1.[26] The spectral resolution of the monochromator was 0.2 eV. The spectra have been measured at room temperature under 5 mbar oxygen pressure using the in situ low-energy XAS setup as developed by Knop-Gericke and coworkers.[9] The X-ray absorption spectral shape is measured with a collector plate that detects the ionized gas that is due to the created electrons in the X-ray absorption process and the subsequent nonradiative decay of the core hole. This ionized gas conversion total electron yield has a probing depth of approximately 4 nm.[27]

2.3. Electron Energy Loss Spectroscopy. The Fe $L_{2,3}$-EELS spectra were collected with a Gatan DigiPEELS 766 parallel electron spectrometer attached to a Philips CM12 TEM operating at 120 kV.[28] Because it was operating in an undersaturated mode, the energy spread of the LaB_6 cathode defined as full width at half-maximum height of the zero-loss peak was 0.8 eV. The spectra were collected in diffraction mode using a 2-mm PEELS aperture at small convergence $a = 2.6$ mrad. The measurements were performed with an energy dispersion of 0.1 eV/channel. We examined 6−12 grains per sample to check the data reproducibility and to exclude errors due to sample inhomogeniety and possible orientation-dependent effects. No sign of radiation damage was observed. Data reduction included the correction for dark current and channel-to-channel gain variation and the subtraction of an inverse power law background. Multiple scattering and tailing effects of the zero-loss peak were deconvoluted by the Fourier-ratio technique[29] using the corresponding low-loss spectra, acquired consecutively to core-loss spectra from the same specimen region.

2.4. Multiplet Calculations. We have applied crystal-field multiplet theory and charge-transfer multiplet theory[1] to calculate K-preedge, L-edge, and 1s2p RIXS spectral shapes. With the crystal-field multiplet theory, the $L_{2,3}$ edge has been calculated with the transition from $3d^5$ to $2p^53d^6$ for Fe^{III}. In addition, charge-transfer multiplet calculations have been carried out using the transition from $3d^5 + 3d^6L$ to $2p^53d^6 + 2p^53d^7L$, where L implies a hole in the oxygen 2p valence band. The K preedge has been calculated as the quadrupole transition from $3d^5$ to $1s^13d^6$ for the octahedral Fe^{III}. In the case of the tetrahedral Fe^{III}, the dipole channel from $3d^5$ to $1s^13d^54p^1$ can be added and coupled to the quadrupole transition, but in the present paper we did not include this option. The 1s2p X-ray emission channel is calculated as the transition from $1s^13d^6$ to $2p^53d^6$ and the 1s2p RIXS is calculated using the Kramers−Heisenberg formula as given above, with $|g\rangle = 3d^5$, $|n\rangle = 1s^13d^6$, and $|f\rangle = 2p^53d^6$. In the case of Fe^{II} systems, an extra 3d electron is added to all states.

2.5. Sample Preparation. We examined four samples, hematite α-Fe_2O_3, hercynite $FeAl_2O_4$, rodolicoite $FePO_4$, and fayalite Fe_2SiO_4 (synthesis, D. Frost, unpublished), that is, respectively, octahedral Fe^{III}, octahedral Fe^{II}, tetrahedral Fe^{III}, and tetrahedral Fe^{II}, which were well characterized for chemical composition and crystal structure by electron microprobe analysis and X-ray diffraction. Synthetic polycrystalline $FeAl_2O_4$ samples were synthesized from Fe_2O_3 (purity 99.99%) and Al_2O_3 (purity 99.99%). The oxide mixtures were mixed in an agate mortar, pelletized, and sintered at 1400 °C in vertical gas mixing furnaces using a $CO/CO_2 = 75/25$ gas mixture. The samples were quenched rapidly, reground, and subsequently reannealed at 1400 °C for 18 h, 1100 °C for 48 h, and 700 for 48 h, always using a $CO/CO_2 = 85/15$ gas mixture. Samples

were characterized using XRD and Mössbauer spectroscopy. Details are given by Klemme and van Miltenburg.[30] For the EELS investigations, TEM specimen are prepared exclusively by crushing small crystals between clean glass slides and suspending tiny fragments with ethanol onto holey TEM grids. For the XANES and RIXS investigations, all of the samples were measured as powders.

3. Results and Discussion

3.1. 1s2p RIXS Spectra. 1s2p RIXS involves the measurement of the 1s2p X-ray emission spectra at the excitation energies related to the 1s preedge energies. This has been discussed in detail in a recent paper by Glatzel and Bergmann.[2] In first approximation, this 1s2p RIXS plane can be understood as the transition from the $3d^6$ ground state to the $2p^53d^7$ final states via the $1s^13d^7$ intermediate states. This resonant transition is described with the Kramers−Heisenberg formula and the matrices involved are the $3d^6 \rightarrow 1s^13d^7$ quadrupole transition coupled to the $1s^13d^7 \rightarrow 2p^53d^7$ dipole decay. One obtains the K preedge structure by looking at the incident energy and integrating over the decay channels, that is, over the emission energy (or equivalently the energy transfer). One obtains the L-edge spectrum by looking at the energy transfer and integrating over the incident energy. Hence, the 1s2p RIXS plane contains information of both K-preedge and L-edge spectra.

Figure 2a shows the experimental 1s2p RIXS spectrum of $FeAl_2O_4$, given as a contour plot. The image on the left indicates the raw data as measured. The image on the right has been created after subtracting the edge structure. The preedge has a maximum intensity at 7113 eV and one observes a maximum emission at energy transfers of 706 eV to 707 eV. A shoulder is visible at 7114.5 eV excitation energy and 708 eV energy transfer. At higher energy, the edge absorption becomes visible above 7118 eV excitation energy and 712 eV energy transfer. Figure 2b shows the 1s2p RIXS spectrum of Fe_2SiO_4, where we note that the contour looks rather similar to the case of $FeAl_2O_4$. Figure 2c shows the 1s2p RIXS spectrum of Fe_2O_3. The contours look rather different from both divalent oxides, and a dominating diagonal structure is visible. A diagonal line indicates that the energy transfer follows the incident energy; in other words, the emission occurs at constant emission energy. Emission at constant energy can relate to nonresonant channels, that is, channels where the information on the excitation is lost (or the photoexcited electron does not interact with the remaining ion) and the decay is given by the same transition for all excitation energies. Another route for obtaining a constant emission energy is a channel that conserves the electronic excitation during the decay step and essentially replaces the 1s core hole with the 2p core hole. This seems to be the most likely explanation for the two crystal-field split peaks at 7114.5 and 7116 eV. They have energy transfer peaks at, respectively, 707.5 and 709 eV, implying that they maintain their crystal-field symmetry during decay. In other words, a t_{2g}-like intermediate state decays preferentially to a t_{2g}-like final state. A faint peak is visible at 7119 eV excitation energy and 712.5 eV energy transfer. As will be discussed below, the nature of this peak is most likely due to mixing with the 3d character of the iron nearest neighbors. Figure 2d shows the experimental 1s2p RIXS spectrum of $FePO_4$. The contours show an essentially single peak, caused by the dominating dipole excitation in $FePO_4$ that has only one transition. Notice that the broadening of the peak is essentially symmetric for the incident energy, but it is highly asymmetric for the energy transfer. This indicates that the final state is not a single state, but that there are additional shoulder

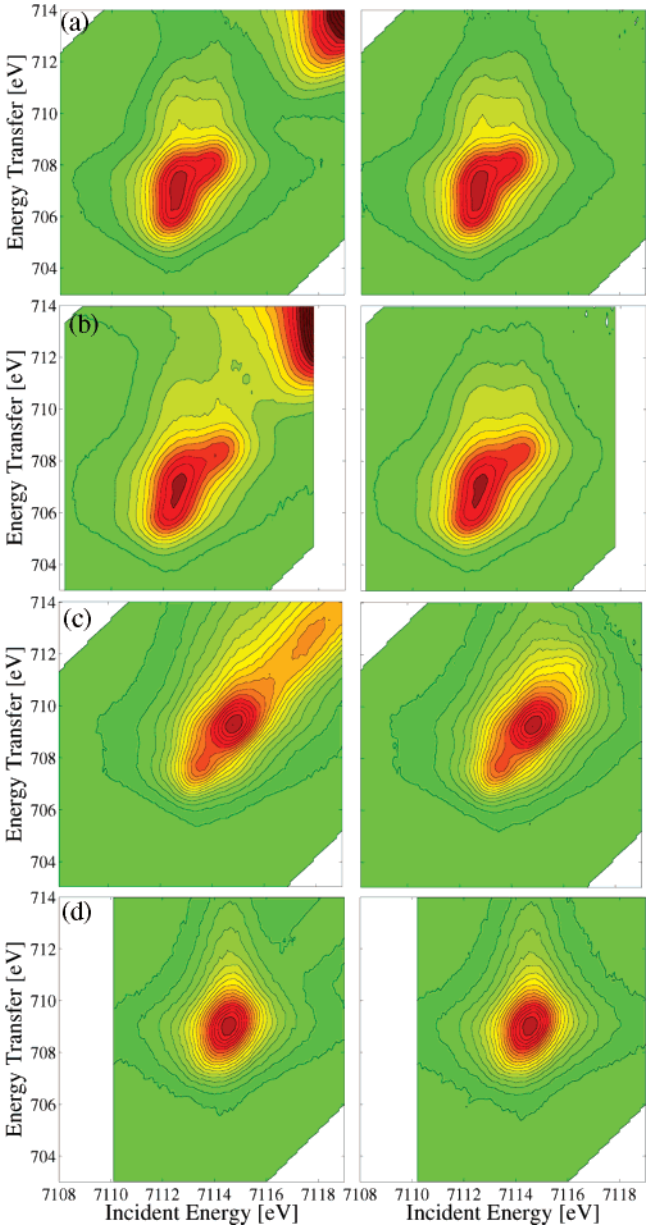

Figure 2. Experimental $1s2p_{3/2}$ RIXS spectrum, given as a contour plot with identical energy scales. The K main edge was subtracted in the plots on the right. The red (dark) area relates to the peak maximum. From top to bottom are, respectively, (a) $FeAl_2O_4$, (b) Fe_2SiO_4, (c) Fe_2O_3, and (d) $FePO_4$.

states at the high energy transfer site of the main peak. The preedge is further separated from the main edge for Fe^{III} states, which implies that the edge itself falls outside the 2D image shown.

Figure 3a shows the theoretical Fe $1s2p_{3/2}$ RIXS spectrum of $FeAl_2O_4$ with an experimental broadening of 1.0 eV for both the monochromator and the detector resolution. The experimental spectrum as given in Figure 2a is essentially reproduced. One observes an extended maximum for the main preedge peak and a second peak at higher excitation energy and higher energy transfer. Figure 3b gives the 1s2p RIXS calculation of Fe_2SiO_4. The calculation is again in agreement with the experiment. It can be seen that the calculations for $FeAl_2O_4$ and Fe_2SiO_4 are similar. Close inspection shows an asymmetry of the main peak of $FeSi_2O_4$. Figure 3c gives the 1s2p RIXS of Fe_2O_3, which has two clearly distinct peaks. This spectrum is significantly different from the experiment. The intensity ratio of the two

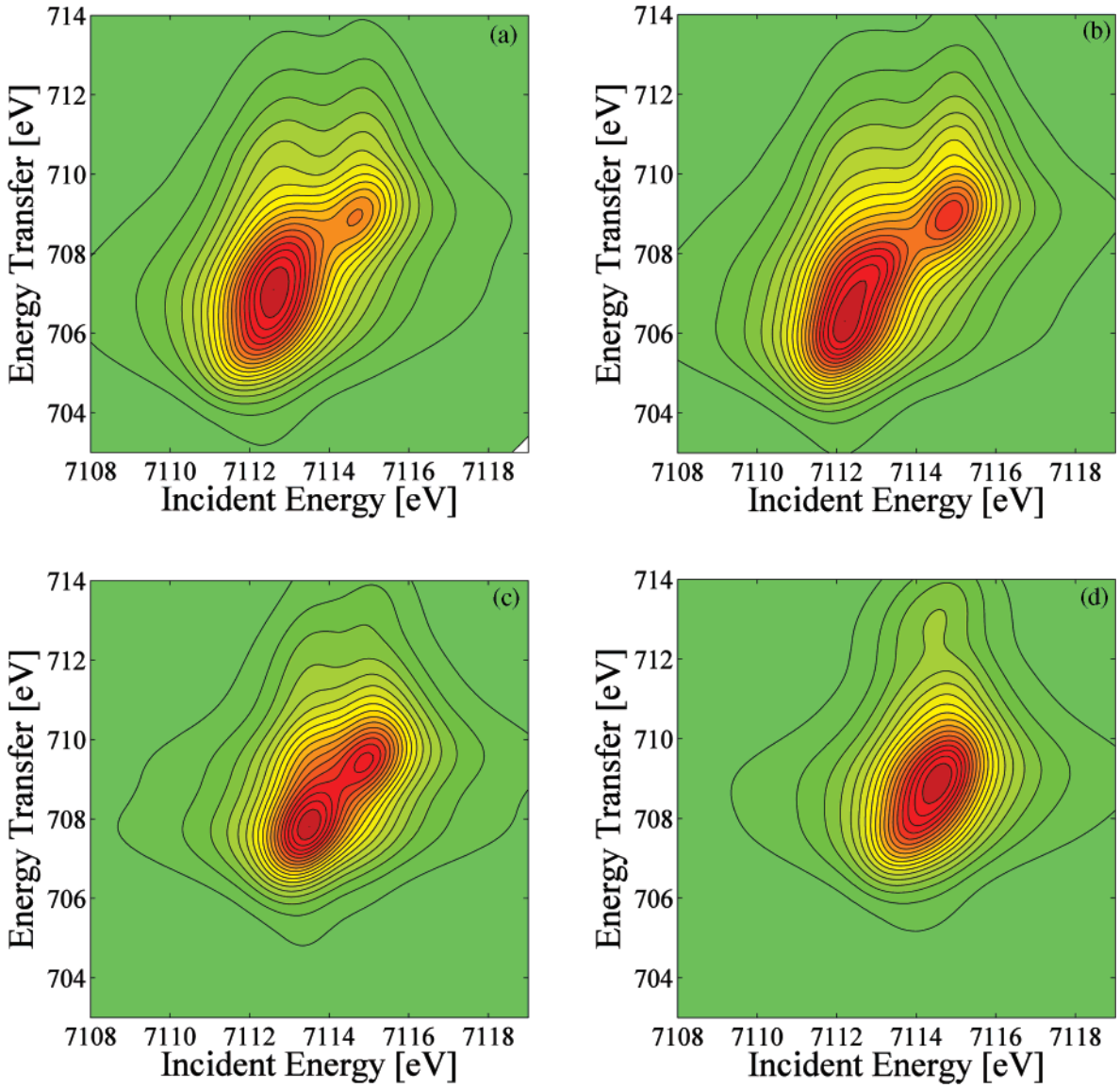

Figure 3. Theoretical $1s2p_{3/2}$ RIXS spectra, given as contour plots. The dark (red) area relates to the peak maximum. (a) $FeAl_2O_4$, (b) Fe_2SiO_4, (c) Fe_2O_3, and (d) $FePO_4$.

peaks, essentially the t_{2g} and the e_g peak, is reversed in experiment with respect to theory. This discrepancy has also been observed by Caliebe et al.[17] In addition, the additional structure between the preedge and the edge is not found in the crystal-field multiplet calculations. Figure 3d gives the 1s2p RIXS of $FePO_4$. A single peak elongated in the energy transfer direction is found similar to that in the experimental spectrum.

The main trends in the 1s2p RIXS can be found from the atomic multiplet transitions for the $3d^6$ (Fe^{II}) and $3d^5$ (Fe^{III}) cases. A $3d^5$ system has only one atomic quadrupole transition from the ^6S ground state to the ^5D final state. A $3d^6$ system has two atomic quadrupole transitions from the ^5D ground state to the ^4F and ^4P final states. These atomic effects are visible in the 1s2p RIXS spectra as the double peak structure for Fe^{II} and the single peak structure for Fe^{III}. The vertical axis shows the 2p final states, which are identical to the final states of 2p XAS. The atomic 2p XAS spectra have their well-known multiplet features, and it is clear that the largest influence on the 1s2p RIXS spectral shape is caused by the atomic multiplet effects. This implies that with a resolution of 1.0 eV for the excitation and 1.0 for the decay, most nonatomic effects such as the crystal-field and charge transfer will not be clearly visible. To better study these effects, one would need an improved resolution of ~0.3 eV, similar to that of 2p XAS.

Figure 4 is a repetition of Figure 3 with the modification of the experimental resolution of monochromator and detector from 1.0 to 0.3 eV. Figure 4a shows the theoretical Fe $1s2p_{3/2}$ RIXS spectrum of $FeAl_2O_4$. It is evident that the increase in information content between Figure 4a and Figure 3a is enormous. The peak at 7113 eV is split into two in the energy transfer direction with peaks at 706 and 707.5 eV. In addition, the peak at 7114.5 eV excitation energy has two decay peaks at, respectively, 709 and 710.5 eV. This figure shows that in order to make full use of the possibilities of 1s2p RIXS an overall experimental resolution of 0.3 eV is needed. For example, with this 0.3 eV resolution the differences between $FeAl_2O_4$ and Fe_2SiO_4 are clear. Fe_2SiO_4 as given in Figure 4b has a broad asymmetric peak at (7112, 706) followed by a more singular peak at (7113, 708), whereas in the case of $FeAl_2O_4$ this is exactly opposite, as visible in Figure 4a. It is important to note that the differences between $FeAl_2O_4$ and Fe_2SiO_4 are larger in 1s2p RIXS planes compared to their 2p XAS spectra, which indicates the superior possibilities of 1s2p RIXS (compared with 2p XAS) to determine the details in the electronic structure.

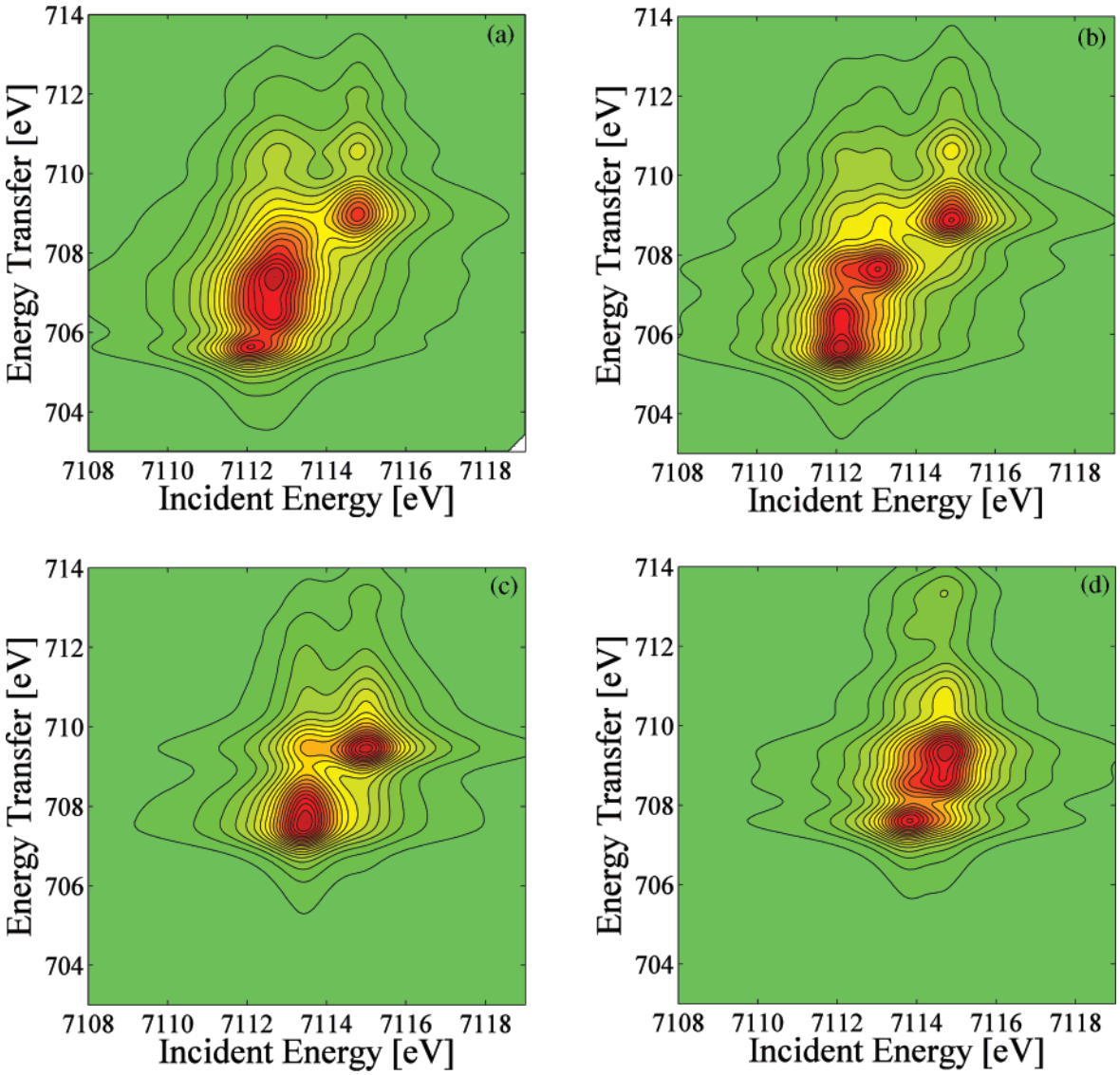

Figure 4. Theoretical $1s2p_{3/2}$ RIXS spectra with an experimental broadening of 0.3 eV for both the monochromator and the detector resolution. The dark (red) area relates to the peak maximum. (a) $FeAl_2O_4$, (b) Fe_2SiO_4, (c) Fe_2O_3, and (d) $FePO_4$.

Fe^{III} compounds have just one single excitation energy for atomic states, hence all fine structure is related to crystal-field effects as well as multiplet effects in the final state. The Fe_2O_3 spectrum has two clearly distinct peaks (that were already visible with the 1.0 eV resolution), but, as discussed this simulation, they differ from those in the experiment. The high-resolution $FePO_4$ spectrum shows clear crystal-field effects, and peaks are visible at (7114, 708) and (7115, 709−709.5), which were only visible as asymmetries in Figure 3.

3.2. Comparison with K-Edge X-ray Absorption Spectra. Figure 5 shows the Fe 1s X-ray absorption spectra of Fe_2SiO_4, $FeAl_2O_4$, Fe_2O_3, and $FePO_4$ normalized to the edge jump with respect to the EXAFS-region. These K edges have been obtained by integrating the 1s2p RIXS planes over the emission energy, the so-called IEE scan. One observes a preedge structure around 7115 eV, followed by the absorption edge. The edge energy is 7118 eV for the divalent iron oxides and 7122 eV for the trivalent iron oxides. The onset of the edges is exactly identical for both divalent and trivalent iron oxides. At higher energies, differences occur between Fe_2SiO_4 and $FeAl_2O_4$ as well as between Fe_2O_3 and $FePO_4$ because of differences in their empty density of states. The edge shift of 4 eV between Fe^{II} and Fe^{III} oxides is in agreement with the trends found in, for example,

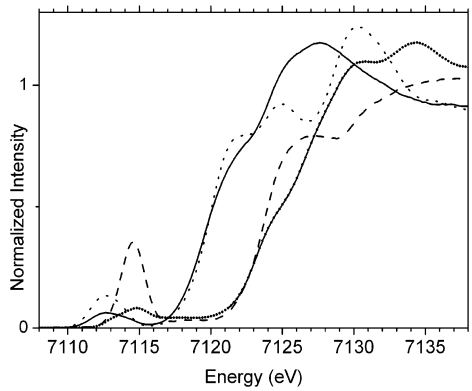

Figure 5. Experimental Fe 1s X-ray absorption spectra of (a) $FeAl_2O_4$ (dotted), (b) Fe_2SiO_4 (solid), (c) Fe_2O_3 (solid with points), and (d) $FePO_4$ (dashed).

bulk Mn oxides.[31] De Vries et al. found from quantum chemical analysis that it is not so much the valence itself, but more the resulting metal−oxygen distances that determine the edge energy in 3d oxides.[32]

Figure 6 shows an enlargement of the preedge features in the K edges of Fe_2SiO_4, $FeAl_2O_4$, Fe_2O_3, and $FePO_4$. These

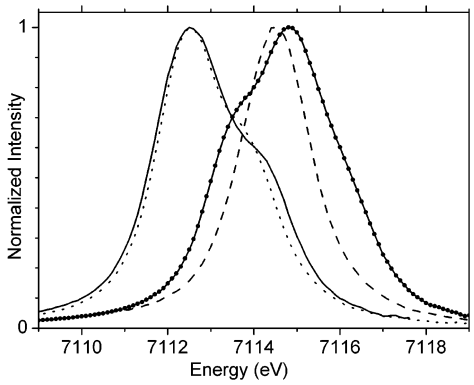

Figure 6. Normalized preedge features of (a) $FeAl_2O_4$ (dotted), (b) Fe_2SiO_4 (solid), (c) Fe_2O_3 (solid with points), and (d) $FePO_4$ (dashed).

spectra have been created from the 1s2p RIXS planes by subtracting the edge structure and by integrating the emission energy. The spectra have been normalized to highlight the differences in their spectral shapes. The preedge energy can be characterized by its center-of-gravity (first moment) and is positioned at 7113 eV for the divalent iron oxides and at 7114.5 eV for the trivalent iron oxides. This shift of 1.5 eV is significantly less than the edge shift of 4 eV, in agreement with the findings of, for example, vanadium oxides.[33] $FePO_4$ exhibits a sharp and strong preedge peak. In the case of the divalent iron oxides, at least two features are visible for each system and the tetrahedral $FeAl_2O_4$ sites give rise to a larger preedge intensity. From the analysis of a large number of iron compounds, the intensity and position of the preedge has been determined using the center-of-gravity method for the position.[34] The results give an average energy position of Fe^{III} preedges at 7113.5 eV for both for tetrahedral and octahedral symmetry, whereas their relative intensities are 0.35 for tetrahedral and 0.06 for octahedral symmetry, respectively. Hence, the main difference is the increased intensity resulting from a much larger dipole contribution to the tetrahedral site. A similar phenomenon can be observed for Fe^{II}, which leads to a tool to analyze both the valence and symmetry of iron sites from the preedge analysis. It has been shown by Heijboer et al. that this analysis can also be applied to Kβ detected spectra.[20]

The preedge region of iron compounds has been investigated systematically by Westre and co-workers.[18] The preedges are analyzed in terms of quadrupole transitions and the spectra could be interpreted in terms of multiplet theory, including the crystal-field and intra-atomic electron−electron interactions. The Fe^{III} spectra are calculated from the quadrupole transitions of $3d^5$ to $1s^13d^6$. The Fe^{II} spectra use $3d^6$ as the ground state. The intensity of the preedge region is much larger for compounds in which the metal site has tetrahedral symmetry than for octahedral systems. In tetrahedral systems, the local mixing of p and d nature is symmetry allowed, whereas for a system with inversion symmetry such as octahedral symmetry it is forbidden. This rule is relaxed in the solid, and if the density of states is calculated then one finds small admixtures of p states into the 3d band even for perfect octahedral systems, for example, $SrTiO_3$.[35] However, this admixture is less than that for tetrahedral systems. P character will be mixed into the 3d band if an octahedral metal site is distorted, resulting in an increased intensity of the preedge. In a recent paper by Arrio and co-workers[36] the preedges are calculated with multiplet theory in low symmetry, allowing for the explicit inclusion of the coupling of the dipole and quadrupole transitions. A number of iron mineral preedge spectra are divided into their dipole or quadrupole nature.

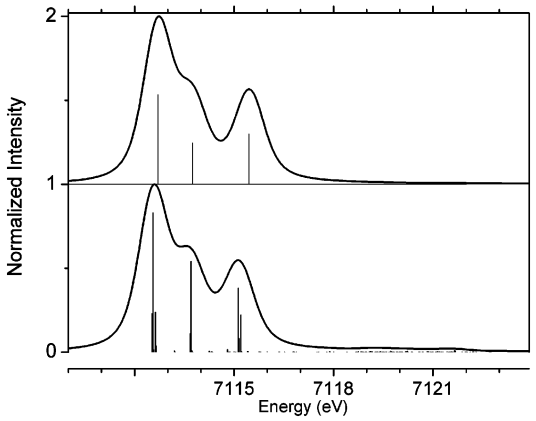

Figure 7. Crystal-field (top) and charge-transfer (bottom) multiplet calculations of the preedge of Fe_2SiO_4.

The assignment of the preedge structures in terms of both quadrupole and dipole transitions yields a uniform and consistent description of the iron K preedge structures. In this analysis, the energies of dipole and quadrupole peaks are assumed to be equal, where this assumption is in agreement with the observation that the peak positions of the octahedral complexes (dominated by quadrupole transitions) are essentially equal to the peak positions of the tetrahedral complexes (dominated by dipole transitions).[18]

Figure 7 shows two multiplet calculations of the preedge of Fe_2SiO_4. The Fe site has a $3d^6$ configuration, which in spherical symmetry has a ^5D ground state. A quadrupole excitation brings this ground state to two possible final states, respectively, ^4F and ^4P. The addition of a cubic crystal-field (top spectrum) gives three peaks, respectively, related to $^4T_{1g}$, $^4T_{2g}$, and another $^4T_{1g}$ final state of the $(1s^1)3d^7$ configurations, where the symmetry labels apply to the 3d part only.[18] These crystal-field multiplet calculations do not include (a) the 3d spin−orbit coupling, (b) the 1s3d exchange interaction, or (c) the effects due to charge transfer. The bottom figure includes all of these effects and instead of three peaks, a large number of peaks are visible. However, after broadening essentially the same spectrum is obtained. Note that at the energy range between 7117 and 7123 eV charge-transfer satellites would be visible in principle, similar to the $L_{2,3}$ edges. In this energy range, one observes the sharply rising main K edge, which makes any small charge transfer satellites impossible to distinguish. For tetrahedral symmetry, there is the well-known admixture of dipole transitions to some (but not all) multiplet states. The full charge transfer multiplet calculations essentially confirm the calculations of Westre et al.[18] For an octahedral Fe^{III} oxide such as Fe_2O_3, one expects a preedge consisting of two peaks split by the crystal field and with an intensity ratio given by the number of empty T_{2g} and E_g states, that is, 3:2. Instead, Fe_2O_3 has a second peak that has a higher instead of a lower intensity than the first peak.

Before going into a possible explanation for this discrepancy, we note that other octahedral Fe^{III} systems have a preedge structure as well as a 1s2p RIXS structure exactly in agreement with the calculations. Figure 8 shows the 1s2p RIXS experiment of iron(III) acetylacetonat ($Fe(acac)_3$). In this coordination complex, the iron is octahedral surrounded by six oxygens, but the difference with Fe_2O_3 is the absence of short Fe−Fe interactions. The 1s2p RIXS of $Fe(acac)_3$ is in excellent agreement with the calculation of octahedral Fe^{III} as given in Figure 3c. Also, the 1s2p RIXS spectrum of the mineral andradite as published by Rueff and co-workers has this shape.[22] In the andradite mineral, there are also no short Fe−Fe distances, which confirms that in the case of Fe_2O_3 this short Fe−Fe

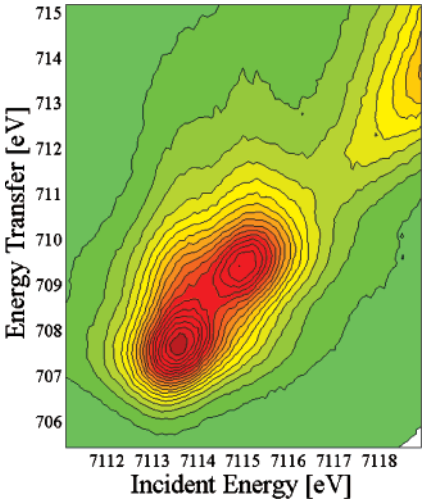

Figure 8. Experimental $1s2p_{3/2}$ RIXS spectrum of $Fe(acac)_3$, given as a contour plot with identical energy scales.

distance is the reason for the discrepancy. A possible mechanism could be the mixing of iron 4p character with the 3d band of a neighboring iron, similar to the case of TiO_2.[37] In the case of Fe_2O_3, this mechanism would lead to a two-peaked quadrupole preedge split by the crystal field plus a two-peaked dipole preedge that is shifted upward by the core hole potential energy of ~3 eV. This second set of structures overlaps with the first set, thereby enhancing the second preedge peak. In addition, this mechanism creates extra intensity between the preedge and the edge. It is our expectation that experimental 1s2p RIXS studies with a resolution of ~0.3 eV will provide evidence to further disentangle these phenomena.

3.3. Comparison with L-Edge X-ray Absorption Spectra. Figure 9 shows the experimental L-edge spectra of the four iron oxides compared to crystal-field multiplet calculations. One observes the transitions from the 2p core state to the empty 3d states. The L_3 edge with transitions to the $2p_{3/2}$ states is visible at 710 eV and the L_2 edge with transitions to the $2p_{1/2}$ states at 722 eV. The 2p core hole wave function has a large overlap with the 3d wave functions, which causes the so-called multiplet effect that causes the 2p X-ray absorption line shapes to be given, in first approximation, by the $2p^53d^6$ (Fe^{III}) and $2p^53d^7$ (Fe^{II}) final states, respectively. The Fe^{III} have their main L_3 peak at 710 eV, whereas for the Fe^{II} systems the peak position is shifted to 708.5 eV. This peak shift of approximately 1.5 eV is, by accident, equivalent to the crystal-field splitting of Fe_2O_3. This crystal-field splitting of 1.5 eV creates the low-energy peak in the Fe_2O_3 spectrum that is also positioned at 708.5 eV. The difference between the Fe_2O_3 and $FePO_4$ spectra is caused by their difference in point group symmetry, octahedral versus tetrahedral, and the associated difference in crystal-field strength. The ground-state electronic symmetry state of both Fe_2O_3 and $FePO_4$ is $^6A_1$ because the five occupied 3d electrons are high-spin and fill the five 3d orbitals, thereby creating a spherical symmetric ground state. The spectra of Fe_2SiO_4 and $FeAl_2O_4$ look rather similar, despite the fact that their ground-state symmetry state is different. They are, respectively, $^5T_2$ for Fe_2SiO_4 and ^5E for $FeAl_2O_4$ because in addition to the five spin-up electrons the sixth electron is spin-down and fills the lowest empty state, the T_{2g} state for Fe_2SiO_4, and the E_g state for

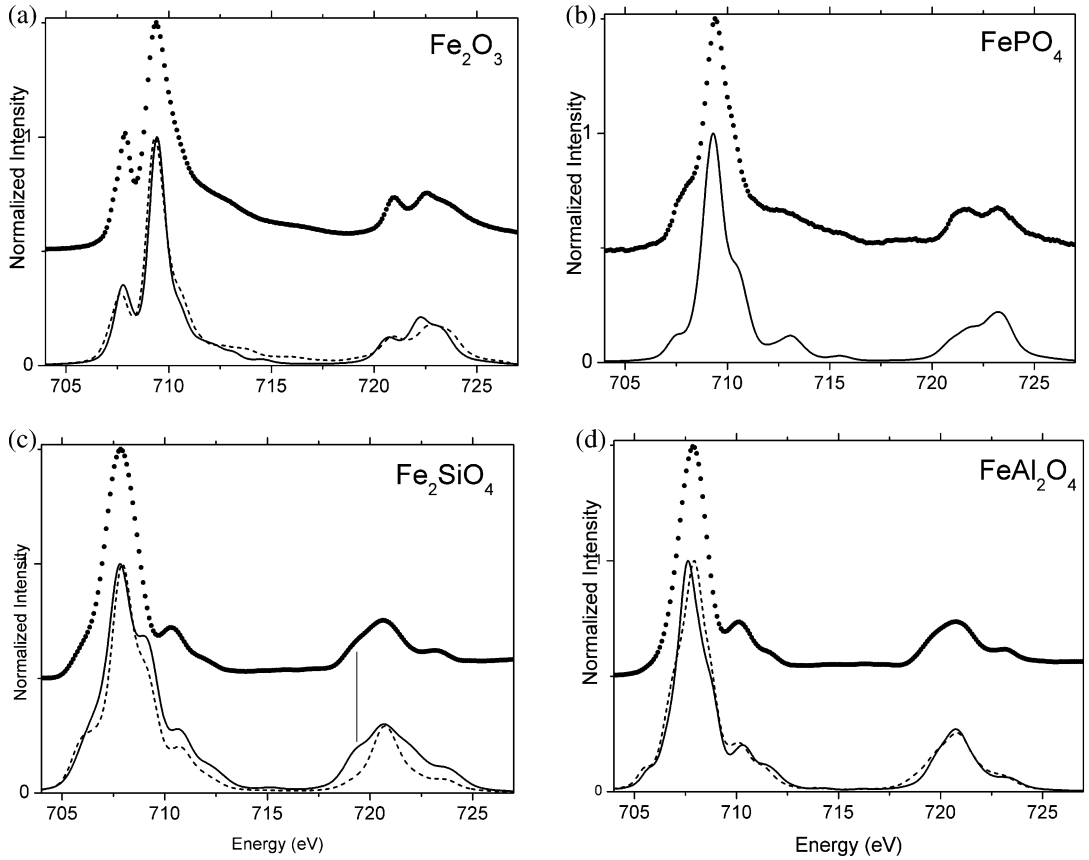

Figure 9. (a) Fe 2p XAS of Fe_2O_3 (points) compared to a crystal-field multiplet calculation (solid) and a charge-transfer multiplet simulation (dashed). The parameters used are given in the text. (b) The Fe 2p XAS of $FePO_4$ (points) compared to a crystal-field multiplet calculation (solid). (c) The Fe 2p EELS spectrum of Fe_2SiO_4 (points) compared to a crystal-field multiplet calculation with 3d spin−orbit coupling (dashed) and without 3d spin−orbit coupling (solid). (d) The Fe 2p EELS spectrum of $FeAl_2O_4$ (points) compared to a crystal-field multiplet calculation in octahedral symmetry (solid) and with a tetragonal distortion (dashed).

$FeAl_2O_4$, respectively. Below we will show that both of these ground states indeed yield a similar 2p X-ray absorption spectrum.

The crystal-field multiplet calculation of Fe_2O_3 is given with a solid line. The crystal-field strength has been set at 1.5 eV and the Slater−Condon parameters (equivalent to the Racah B parameter) have been rescaled to 90% of their atomic values.[1] The L_3 part of the spectrum has been broadened with a 0.4 eV (full width half-maximum (fwhm)) Lorentzian and the L_2 part with a 0.8 eV Lorentzian to account for the additional Coster−Kronig decay channels. A Gaussian broadening of 0.5 eV has been added to match the experimental resolution. The simulation describes the experimental spectrum well for both the L_3 edge and the L_2 edge. Some small deviations are that the peak intensity at 708 eV is calculated too low, which is a result that is well known in crystal-field multiplet simulations of iron oxides.[38] At the L_2 edge, the first peak is too low and the peak positions are off by ~0.2 eV. Crystal-field multiplet calculations are only a first approximation to simulate the experimental spectra, and many effects are not included in such calculations. It has been shown that the inclusion of the $3d^6L$ configuration improves the simulation of some 2p X-ray absorption spectra significantly, in particular for trivalent and tetravalent systems. From a series of charge-transfer calculations using a $3d^5 + 3d^6L$ ground state, we found that an overall crystal-field splitting of 1.5 eV can be obtained by including an ionic crystal-field splitting of 1.2 eV, with an additional 0.3 eV splitting due to the difference of hopping energies of 1.0 eV (t_{2g}) and 2.0 eV (e_g) respectively.[39] The energy difference between the $3d^5$ and $3d^6L$ configuration (i.e., the charge-transfer energy) has been set to 3.0 eV. This simulation is given with the dashed line. It can be seen that the charge-transfer simulation does not solve the discrepancy of the first peak, but it does produce the correct splitting between the L_3 and L_2 edge. In addition, the satellites at ~713 eV and ~717 eV are found in the simulation. Because the improvement of including charge transfer to the spectral shape of Fe_2O_3 is not very large and because the effects of charge transfer will be even smaller for the other three oxides, we decided to use only the crystal-field multiplet approach for all calculations. This also limits the degrees of freedom for the spectral simulations.

The spectrum of $FePO_4$ has been simulated with a crystal field of −0.9 eV and the Slater−Condon parameters rescaled 90% of their atomic value. A negative crystal-field value indicates that the energy position of the e states is below the t_2 states. The simulated spectrum agrees well with the experiment. The energy positions of the leading peak at 708 eV, the peak at 713 eV, and that at 716 eV are all reproduced. The spectrum of Fe_2SiO_4 is calculated with a crystal-field strength of 1.2 eV and atomic Slater−Condon parameters have been used. The $^5T_2$ ground state of Fe_2SiO_4 is sensitive to the effects of 3d spin−orbit coupling, similar to other 3d oxides such as CoO[1] and $LaNiO_3$.[40] We have calculated the Fe_2SiO_4 spectrum with and without spin−orbit coupling. At the L_3 edge, there is no clear distinction in the calculations, but the L_2 edge is much better simulated if 3d spin−orbit coupling is not included. In particular, the peak at 719 eV is observed clearly in experiment and is absent if 3d spin−orbit coupling is included. Therefore, we conclude that for Fe_2SiO_4 the 3d spin−orbit coupling is effectively quenched at room temperature, which could be caused by dispersion effects and/or by symmetry reduction. The spectrum of $FeAl_2O_4$ is calculated with a crystal-field strength of −0.7 eV. The calculation in octahedral symmetry (solid line) describes the experimental spectrum rather well. The ground-state symmetry of a tetrahedral Fe^{II} site is ^5E and the e-orbital is partly filled, giving rise to a Jahn−Teller distortion. We have also calculated the 2p X-ray absorption spectrum after applying a small tetragonal field (Ds = 0.1 eV). The dashed line gives a more symmetric L_3 main edge, improving the agreement with experiment, and also the L_2 edge seems better described. The parameters determined from the 2p XAS spectral shapes have also been used for the 1s2p RIXS calculations.

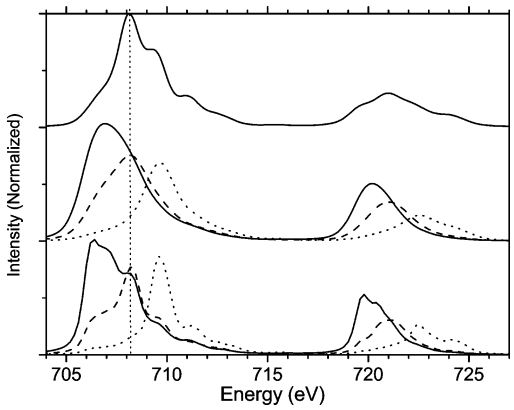

Figure 10. Fe 2p XAS calculation of Fe_2SiO_4 (top) compared to three cross sections through the theoretical 1s2p RIXS plane using the present resolution of 1.0 eV (middle) and the needed resolution of 0.3 eV (bottom). Identical ground-state parameters are used. The three CIE cross sections, or resonant X-ray emission spectra, have been set to 7112 eV (solid), 7113 eV (dashed) and 7114.6 eV (dotted).

Figure 10 compares the 2p XAS spectrum of Fe_2SiO_4 with CIE cross sections through the 1s2p RIXS plane. The 2p XAS spectrum shows a peak at 708 eV and a shoulder at 709.5 eV. The CIE cross section at 7112 eV shows two peaks at 706 and 707 eV, which implies that different final states are probed. The 7113 eV spectrum shows its main peak at 708 eV and roughly the same peaks are seen as in 2p XAS with slightly different intensities. These two CIE spectra relate essentially to the first $^4T_{1g}$ and $^4T_{2g}$ of the $(1s^1)3d^7$ states in the K preedge (as given in Figure 7). The reason that the 1s2p resonant XES spectrum of the $^4T_{2g}$ intermediate state peak looks like direct 2p XAS is caused by the fact that the overall symmetry of this intermediate state is $^4T_2$ times ^2S, yielding $^5T_2$ symmetry ($^3T_2$ is not allowed). This is the same symmetry as the ground state. The 2p XAS process then brings the $^5T_2$ ground state to $^5T_1$ times ^1P final states. Similarly, the 1s2p XES brings the $^5T_2$ intermediate state to final states of the same symmetry, but because of the different matrix elements they have different spectra. The third peak at 7114.6 eV peaks at 710 eV in the final state. One observes a diagonal trend, as also is visible in the 1s2p RIXS planes. The quadrupole excitation reaches different multiplet states in the K preedge, and these states maintain the energy difference in their decay process. This applies to spin (high-spin at the lowest energy) and crystal-field effects (T_2 at the lowest energies). If one includes charge transfer, then it also applies to charge-transfer excitations.

The 1.0 eV broadened spectra of course give the same trend, but most of the fine structure has disappeared. The experimental spectra are equivalent to these 1.0 eV theoretical spectra. Because of a lack of fine structure, it is not possible to derive the crystal-field and other parameters with the same accuracy as that for 2p XAS spectra. This clearly demonstrates that if one would like to use 1s2p RIXS for electronic structure determinations, similar to 2pXAS, one needs an overall resolution of the order of 0.3 eV. This will yield a characterization method that is even more powerful than 2p XAS because a number of different resonant 1s2p XES spectra can be obtained,

which together will allow a more reliable multiplet fit, yielding the crystal-field (and charge-transfer) parameters. These resonant 1s2p XES spectra involve only hard X-rays and therefore allow for experiments under essentially any (extreme) condition. Together this opens a new versatile and powerful tool for in situ electronic structure determinations for transition metals, which will likely have many applications in fields such as catalysis, fuel cells, batteries and geoscience.

Conclusions

We hope that with this paper we have added to the development of new, more quantitative ways of measuring and interpreting preedge structures. There are undoubtedly many effects hidden in the preedge spectral region, some of which could be very valuable in characterizing the electronic and molecular structure of 3d transition-metal systems. RIXS experiments have the potential to "circumvent" the limitation given by lifetime broadening and the large background from the main absorption edge. A practical advantage, in particular, of 1s2p RIXS is the fact that these experiments, unlike conventional 2p XAS, make use of a hard X-ray probe. This implies that experiments under extreme conditions and in chemical reactors or other in situ situations will benefit most from the possibilities from 1s2p RIXS.[2] Similarly, metalloproteins that are sensitive to photoreduction or photooxidation profit from the less-damaging hard X-ray probe. Here the most well-known example might be the Mn cluster of the oxygen-evolving complex in photosystem II. In the data shown in this paper, the main limitation has been the overall energy resolution, which has prevented us from gaining more detailed information. Nevertheless, even with somewhat poorer resolution, useful information such as the valence and spin state has been determined with RIXS, for example, under extreme conditions.[41] Energy resolution is not a fundamental limitation of this technique. In fact, high-resolution data have been reported already several years ago (see, e.g., ref 17). At present, RIXS beamlines exist or are being designed at, for example, the ESRF, APS, SPRING8, PETRA III, SOLEIL, and DIAMOND storage rings. The challenge for these future instruments is to combine high resolution with good sensitivity in order to make it practical to measure a complete RIXS plane in a reasonable time even for dilute systems or difficult conditions. Such work is in progress and it is expected that in the future additional electronic structure information can be obtained by this potentially powerful technique.

Acknowledgment. We thank the BioCAT and Advanced Photon Source staff for their support during the measurements at Argonne National Laboratories. Use of the APS was supported by the U.S. Department of Energy, Basic Energy Sciences, Office of Science under contract no. W-31-109-ENG-38. BioCAT is a National Institutes of Health-supported Research Center RR-08630. Portions of this research were carried out at the Stanford Synchotron Radiation Laboratory, a national user facility operated by Stanford University on behalf of the U.S. Department of Energy, Office of Basic Energy Sciences. The research of W.M.H. and P.G. is supported by grants from the Netherlands Scientific Organization-Chemical-Sciences (NWO-CW) and the research of FMFdG is supported by the Netherlands Research School Combination on Catalysis (NRSCC) and by a Science-Renewal Fund of NWO-CW.

References and Notes

(1) Degroot, F. M. F. *J. Elec. Spec*. **1994**, *67*, 529.
(2) deGroot, F. *Coord. Chem. Rev*. **2005**, *249*, 31.
(3) Cramer, S. P.; Ralston, C. Y.; Wang, H. X.; Bryant, C. *J. Elec. Spec*. **1997**, *86*, 175.
(4) Wilke, M.; Farges, F.; Petit, P. E.; Brown, G. E.; Martin, F. *Am. Mineral*. **2001**, *86*, 714.
(5) (a) Gloter, A.; Douiri, A.; Tence, M.; Colliex, C. *Ultramicroscopy* **2003**, *96*, 385. (b) Mitterbauer, C.; Kothleitner, G.; Grogger, W.; Zandbergen, H.; Freitag, B.; Tiemeijer, P.; Hofer, F. *Ultramicroscopy* **2003**, *96*, 469.
(6) van Aken, P. A.; Lauterbach, S. *Phys. Chem. Miner*. **2003**, *30*, 469.
(7) Degroot, F. M. F.; Fuggle, J. C.; Thole, B. T.; Sawatzky, G. A. *Phys. Rev. B* **1990**, *41*, 928.
(8) Degroot, F. M. F.; Fuggle, J. C.; Thole, B. T.; Sawatzky, G. A. *Phys. Rev. B* **1990**, *42*, 5459.
(9) (a) Knop-Gericke, A.; Havecker, M.; Neisius, T.; Schedel-Niedrig, T. *Nucl. Instrum. Methods A* **1998**, *406*, 311. (b) Knop-Gericke, A.; Havecker, M.; Schedel-Niedrig, T.; Schlogl, R. *Top. Catal*. **2000**, *10*, 187.
(10) (a) Wagner, J. B.; Hansen, P. L.; Molenbroek, A. M.; Topsoe, H.; Clausen, B. S.; Helveg, S. *J. Phys. Chem. B* **2003**, *107*, 7753. (b) Hansen, P. L.; Wagner, J. B.; Helveg, S.; Rostrup-Nielsen, J. R.; Clausen, B. S.; Topsoe, H. *Science* **2002**, *295*, 2053.
(11) Meitzner, G.; Bare, S. R.; Parker, D.; Woo, H.; Fischer, D. A. *Rev. Sci. Instrum*. **1998**, *69*, 2618.
(12) Hamalainen, K.; Kao, C. C.; Hastings, J. B.; Siddons, D. P.; Berman, L. E.; Stojanoff, V.; Cramer, S. P. *Phys. Rev. B* **1992**, *46*, 14274.
(13) (a) Glatzel, P.; Jacquamet, L.; Bergmann, U.; de Groot, F. M. F.; Cramer, S. P. *Inorg. Chem.* **2002**, *41*, 3121. (b) Glatzel, P.; de Groot, F. M. F.; Manoilova, O.; Grandjean, D.; Weckhuysen, B. M. Bergmann, U.; Barrea, R. *Phys. Rev. B* **2005**, *72*, 014117.
(14) (a) Stojanoff, V.; Hamalainen, K.; Siddons, D. P.; Hastings, J. B.; Berman, L. E.; Cramer, S.; Smith, G. *Rev. Sci. Instrum*. **1992**, *63*, 1125. (b) Bergmann, U.; Grush, M. M.; Horne, C. R.; DeMarois, P.; Penner-Hahn, J. E.; Yocum, C. F.; Wright, D. W.; Dube, C. E.; Armstrong, W. H.; Christou, G.; Eppley, H. J.; Cramer, S. P. *J. Phys. Chem. B* **1998**, *102*, 8350. (c) Schulke, W.; Kaprolat, A.; Fischer, T.; Hoppner, K.; Wohlert, F. *Rev. Sci. Instrum*. **1995**, *66*, 2446.
(15) (a) de Groot, F. *Chem. Rev*. **2001**, *101*, 1779. (b) Butorin, S. M. *J. Elec. Spec*. **2000**, *110*, 213. (c) Kotani, A.; Shin, S. *Rev. Mod. Phys*. **2001**, *73*, 203. (d) Gel'mukhanov, F.; Agren, H. *Phys. Rep*. **1999**, *312*, 91.
(16) Cramer, S. P.; Degroot, F. M. F.; Ma, Y.; Chen, C. T.; Sette, F.; Kipke, C. A.; Eichhorn, D. M.; Chan, M. K.; Armstrong, W. H.; Libby, E.; Christou, G.; Brooker, S.; McKee, V.; Mullins, O. C.; Fuggle, J. C. *J. Am. Chem. Soc*. **1991**, *113*, 7937.
(17) Caliebe, W. A.; Kao, C. C.; Hastings, J. B.; Taguchi, M.; Uozumi, T.; de Groot, F. M. F. *Phys. Rev. B* **1998**, *58*, 13452.
(18) Westre, T. E.; Kennepohl, P.; Dewitt, J. G.; Hedman, B.; Hodgson, K. O.; Solomon, E. I. *J. Am. Chem. Soc*. **1997**, *119*, 6297.
(19) Glatzel, P.; Bergmann, U.; Gu, W. W.; Wang, H. X.; Stepanov, S.; Mandimutsira, B. S.; Riordan, C. G.; Horwitz, C. P.; Collins, T.; Cramer, S. P. *J. Am. Chem. Soc*. **2002**, *124*, 9668.
(20) Heijboer, W. M.; Glatzel, P.; Sawant, K. R.; Lobo, R. F.; Bergmann, U.; Barrea, R. A.; Koningsberger, D. C.; Weckhuysen, B. M.; de Groot, F. M. F. *J. Phys. Chem. B* **2004**, *108*, 10002.
(21) Glatzel, P.; Bergmann, U.; Yano, J.; Visser, H.; Robblee, J. H.; Gu, W. W.; de Groot, F. M. F.; Christou, G.; Pecoraro, V. L.; Cramer, S. P.; Yachandra, V. K. *J. Am. Chem. Soc.* **2004**, *126*, 9946.
(22) Rueff, J. P.; Journel, L.; Petit, P. E.; Farges, F. *Phys. Rev. B* **2004**, *69*, 235107.
(23) Barrea, R. A.; Fischetti, R.; Stepanov, S.; Rosenbaum, G.; Kondrashkina, E.; Bunker, G. B.; Black, E.; Zhang, K.; Gore, D.; Heurich, R.; Vukonich, M.; Kropf, A. J.; Wang, S.; Irving, T. C. *Phys. Scr*. **2005**, *115*, 867.
(24) Bergmann, U.; Cramer, S. P. *SPIE Proc*. **1998**, *3448*, 198.
(25) Troger, L.; Arvanitis, D.; Baberschke, K.; Michaelis, H.; Grimm, U.; Zschech, E. *Phys. Rev. B* **1992**, *46*, 3283.
(26) (a) Follath, J. A. R.; Senf, F. *Nucl. Instrum. Methods A* **1997**, *390*, 388. (b) Senf, F.; Sawhney, K. J. S. *Nucl. Instrum. Methods A* **2001**, *467*−*468*, 466.
(27) Abbate, M.; Goedkoop, J. B.; de Groot, F. M. F.; Grioni, M.; Fuggle, J. C.; Hofmann, S.; Petersen, H.; Sacchi, M. *Surf. Interface Anal*. **1992**, *18*, 65.
(28) Vanaken, P. A.; Wu, Z. Y.; Langenhorst, F.; Seifert, F. *Phys. Rev. B* **1999**, *60*, 3815.
(29) Egerton, R. F. *Electron Energy-Loss Spectroscopy in the Electron Microscope*, 2nd ed.; Plenum Press: New York, 1996.
(30) Klemme, S.; van Miltenburg, J. C. *Am. Miner*. **2003**, *88*, 68.
(31) Subias, G.; Garcia, J.; Proietti, M. G.; Blasco, J. *Phys. Rev. B* **1997**, *56*, 8183.
(32) de Vries, A. H.; Hozoi, L.; Broer, R. *Int. J. Quantum Chem*. **2003**, *91*, 57.
(33) Wong, J.; Lytle, F. W.; Messmer, R. P.; Maylotte, D. H. *Phys. Rev. B* **1984**, *30*, 5596.

(34) Wilke, M.; Farges, F.; Petit, P. E.; Brown, G. E.; Martin, F. *Am. Miner*. **2001**, *86*, 714.

(35) Abbate, M.; Pen, H.; Czyzyk, M. T.; Degroot, F. M. F.; Fuggle, J. C.; Ma, Y. J.; Chen, C. T.; Sette, F.; Fujimori, A.; Ueda, Y.; Kosuge, K. *J. Elec. Spec.* **1993**, *62*, 185.

(36) Arrio, M. A.; Rossano, S.; Brouder, C.; Galoisy, L.; Calas, G. *Europhys. Lett.* **2000**, *51*, 454.

(37) Cabaret, D.; Joly, Y.; Renevier, H.; Natoli, C. R. *J. Synchrotron Radiat.* **1999**, *6*, 258.

(38) (a) Kuiper, P.; Searle, B. G.; Rudolf, P.; Tjeng, L. H.; Chen, C. T. *Phys. Rev. Lett.* **1993**, *70*, 1549. (b) Crocombette, J. P.; Pollak, M.; Jollet, F.; Thromat, N.; Gautiersoyer, M. *Phys. Rev. B* **1995**, *52*, 3143.

(39) Wasinger, E. C.; de Groot, F. M. F.; Hedman, B.; Hodgson, K. O.; Solomon, E. I. *J. Am. Chem. Soc.* **2003**, *125*, 12894.

(40) (a) Piamonteze, C.; Tolentino, H. C. N.; Vicentin, F. C.; Ramos, A. Y.; Massa, N. E.; Alonso, J. A.; Martinez-Lope, M. J.; Casais, M. T. *Surf. Rev. Lett.* **2002**, *9*, 1121. (b) Piamonteze, C.; de Groot, F. M. F.; Tolentino, H. C. N.; Ramos, A. Y.; Massa, N. E.; Alonso, J. A.; Martínez-Lope, M. J. *Phys. Rev. B* **2005**, *71*, 020406.

(41) (a) Rueff, J. P.; Kao, C. C.; Struzhkin, V. V.; Badro, J.; Shu, J.; Hemley, R. J.; Hao, H. K. *Phys. Rev. Lett.* **1999**, *82*, 3284. (b) Badro, J.; Rueff, J. P.; Vanko, G.; Monaco, G.; Fiquet, G.; Guyot, F. *Science* **2004**, *305*, 383.